Effect of Velocity-Slip Boundary Conditions on Jeffery–Hamel Flow Solutions

M. A. Al-Nimr
Department of Mechanical Engineering,
Jordan University of Science and Technology,
Irbid 22110, Jordan

Vladimir A. Hammoudeh

M. A. Hamdan

Department of Mechanical Engineering,
University of Jordan,
Amman 11942, Jordan

In the present work, the Jeffery–Hamel flow problem has been studied using both first- and second-order velocity-slip models, and then compared with the no-slip model. The objectives are to observe the behavior of the flow predicted by the two slip models and to establish criteria for using the two velocity-slip models. The study concentrates on examining the effect of the change in the Knudsen number (Kn) on the velocity profiles, magnitude of slip at the wall, and skin friction coefficient. Assuming that a difference between the two slip models of the order of 10% or less justifies the use of the simple first-order model, the transitional Kn numbers have been found. These Kn numbers depend on the flow direction, being either inflow or outflow. Also, there are three distinct regions that specify where to use each of the no-slip, first-order, and second-order slip models. Further, the reversal of the flow has been investigated as a function of the Kn number and for different $Re \cdot \alpha$, where Re is Reynolds number and α is the wall angle. Using the second-order slip models, it is found that as the Kn number increases, reversal occurs at $Re \cdot \alpha$ smaller than the 10.31 value at which flow reversal happens in the no-slip model, and increasing the Kn number leads to a reduction in the skin friction coefficient in all cases except when reversal occurs. [DOI: 10.1115/1.4000918]

1 Introduction

In the recent years, industries, driven by the constant quest for miniaturization of gadgets and machines, have developed a number of manufacturing processes that can create extremely small electronic and mechanical components. These small devices for which the characteristic length falls in the range between 1 mm and 1 μm are usually referred to as microelectromechanical systems (MEMS). Some of them are very complex systems that combine electrical and mechanical components. Applications of such small devices can nowadays be found in the electronic industries, for example, in ink jet printing, where micropumps deliver picoliters of ink through microscopic nozzles. Another potential application is in electronic equipment cooling, where scientists are experimenting on microheat sinks, which can be integrated into the chips to cool the new power hungry microprocessors. This has led to the increase in interest in the microscale fluid and heat transfer research. It was observed that in such small devices, the fluid flows differ from those in macroscopic machines and cannot always be predicted from conventional flow models such as the Navier–Stokes equations with no-slip boundary condition at a fluid-solid interface. Slip flow, thermal creep, rarefaction, viscous dissipation, compressibility, intermolecular forces, and other unconventional effects may have to be taken into account. For gases, microfluid mechanics has been studied by incorporating slip boundary conditions, thermal creep, viscous dissipation as well as compressibility effects into the continuum equations of motion, but it has a number of limitations. Molecular-based models have also been attempted for certain ranges of the operating parameters.

Since the continuum model is better known and is mathematically easier to handle than alternative molecular models, it should be used as long as it is applicable. That is why in recent years, there has been extensive examination of the validity of the Navier–Stokes equations for the new cases that face the scientists. This examination work can be done both theoretically and experimentally. All these works have shown that the continuum model is fairly accurate as long as local properties such as density and velocity can be defined as averages over elements that are large compared with the microscopic structure of the fluid, but small enough in comparison with the scale of the macroscopic phenomena to permit the use of differential calculus to describe them. Additionally, the flow must not be too far from thermodynamic equilibrium [1].

In order to be able to solve the Navier–Stokes equations for any flow situation, a number of initial and boundary conditions need to be applied. Here, the Knudsen number definition has to be introduced as the ratio between the mean free path (λ) and the characteristic length (L), and is generally the most important parameter determining the flow regime. The different Knudsen number regimes are specific for each geometry and flow configuration, and so they are determined empirically only to serve as a general guidelines for the use of the different models. Based on a number of experimental and theoretical works, it has been established that the traditional no-slip/no-jump boundary conditions give accurate results for the range of $Kn < 0.001$. At larger values of Kn the assumption of equilibrium at the fluid-solid interface is no longer true, and some velocity slip and temperature jump occurs so the model has to be modified in order to take then into consideration. The flow in microchannels falls into the later category, so the modified velocity-slip/temperature-jump models should be used. Navier–Stokes equations with first-order velocity-slip/temperature-jump are considered to be applicable for the range between $0.001 < Kn < 0.1$. For the transition region, which falls in the range between $0.1 < Kn < 10$, there are two options, either by using the Navier–Stokes equations, which can still be applied if second or higher order slip/jump boundary conditions are applied, or by using one of the molecular-based models proposed in the literature.

In the last few years, the increased interest in the microflow area research has resulted in a large number of publications on the subject [2–32]. Gad-el-Hak [5,6] published a couple of reviews, which serve as an excellent introduction into the microflow area of research, while "The Handbook of MEMS," [7] also edited by Gad Al-Hak, presents a must have reference for anyone interested

Contributed by the Applied Mechanics Division of ASME for publication in the JOURNAL OF APPLIED MECHANICS. Manuscript received June 26, 2009; final manuscript received November 18, 2009; published online April 12, 2010. Assoc. Editor: Nesreen Ghaddar.

in the microflow area. Another work presenting an interesting historical overview and deeper physical understanding of the slip boundary condition has been published by Lauga [8]. A summary of the experiments that has been conducted to investigate the behavior of fluid flow in microchannels, over a large range of Reynolds numbers, geometries, and experimental conditions, is presented in Table 6.3 of "The Handbook of MEMS" [7]. As it is clear from this review, the available experimental investigations focus on validating the slip and jump models, and their abilities to describe the hydrodynamics and thermal behaviors of the fluid flow in circular, rectangular, and trapezoidal microchannels [15–29].

Geometrical differences were emphasized in the experiments in Ref. [15], which employed circular glass and silicon microchannels with rectangular, trapezoidal, and triangular cross sections. Comparison of numerical calculations for flow in trapezoidal channels finds good agreement between the numerical and experimental results for $\mathrm{Re}<600$, although some entrance effects were observed in the shortest channels [16]. Microscale measurements of the friction factor conducted in Ref. [17] generally agree with the macroscale laminar theory to within $\pm 2\%$ experimental error over all Reynolds numbers up to transition. Many studies [18–23] find an increase in the friction factor on the microscale level under certain conditions. In some cases, the departure from agreement with theoretical predictions is reasonably linked with a change in the roughness or geometrical parameter. Another group of studies found the flow resistance to be less than the theoretical macroscale predictions for certain conditions [19,24–28]. In Ref. [19], the friction factor was found to be lower than the macroscale theoretical prediction for two out of seven cases. Pfahler et al. [25–27] found the measured friction factors to be lower than theoretical values in many cases when using different working fluids. Choi et al. [24] measured the surface roughness and heat transfer coefficients for nitrogen gas flowing through microtubes with diameters in the range of $3-81$ μm and length to diameter ratios of 640–8100. Yu et al. [28] conducted a similar study of flows through microtubes with diameters of $19-102$ μm and obtained extremely high Reynolds numbers for microscale conditions, up to 20,000. In a couple of newer works, Pozrikidis [29,30] studied the slip boundary conditions in a number of shear flow cases and the effect of the geometry on the velocity slip.

However, due to the variety of problems and approaches, there are still a number of problems that have not been addressed. The scope of the present work should be to investigate the effect of implementing the velocity-slip boundary conditions on the case of radial flow caused by a line source or sink. This problem is discussed by Jeffery [33] and independently by Hamel [34]. Up to our knowledge, so far the Jeffery–Hamel flow has not been investigated in microdomains but we think the study of the behavior of the flow in microconverging/diverging channels will be useful in the study of micronozzles and diffusers. The objective is to investigate the effect of both the first- and second-order slip models on the hydrodynamic behavior of microconvergent/divergent channels. This is attained by establishing criteria that justifies the use of the first-order slip model instead of the second-order slip model.

2 Mathematical Formulation

Referring to the schematic diagram shown in Fig. 1, the flow is considered in polar coordinates (r,θ), generated by a source (or sink) at the origin and bounded by solid walls at $\theta=\pm\alpha$. Assuming that the flow is purely radial, $u_\theta=0$ and from the continuity equation in polar coordinates

$$\frac{1}{r}\frac{\partial}{\partial r}(ru_r)=0 \quad \text{or} \quad ru_r=fcn(\theta) \tag{1}$$

It is expected that u_r will have a local maximum $u_{\max}$ at $\theta=0$. Then a convenient nondimensionalization for this problem is

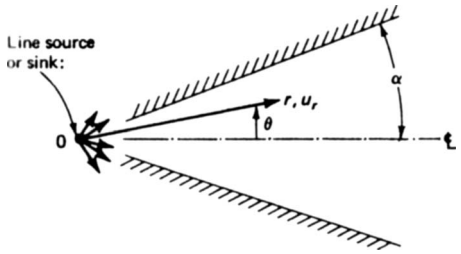

Fig. 1 Schematic diagram of the problem [12]

$$\eta=\frac{\theta}{\alpha}, \quad \frac{u_r}{u_{\max}}=f(\eta) \tag{2}$$

The momentum equations in polar coordinates for $u_\theta=0$ are

$$u_r\frac{\partial u_r}{\partial r}=-\frac{1}{\rho}\frac{\partial \rho}{\partial r}+\nu\left(\frac{\partial^2 u_r}{\partial r^2}+\frac{1}{r}\frac{\partial u_r}{\partial r}-\frac{u_r}{r^2}+\frac{1}{r^2}\frac{\partial^2 u_r}{\partial \theta^2}\right) \tag{3a}$$

$$0=-\frac{1}{\rho r}\frac{\partial p}{\partial \theta}+\frac{2\nu}{r^2}\frac{\partial u_r}{\partial \theta} \tag{3b}$$

The pressure can be eliminated by cross-differentiation and introducing the variables η and $f(\eta)$. The result is a third-order nonlinear differential equation for f

$$f'''+2\mathrm{Re}\cdot\alpha ff'+4\alpha^2 f'=0 \tag{4}$$

where the characteristic Reynolds number of the flow is defined as

$$\mathrm{Re}=\frac{u_{\max} r\alpha}{v} \tag{5}$$

The boundary conditions are assumed symmetric flow with a maximum at the centerline

$$f(0)=1 \tag{6}$$

and the velocity-slip boundary conditions at the wall are as follows:

For the first-order slip model

$$f(-1)=f(+1)=-\frac{2-\sigma_v}{\sigma_v}\mathrm{Kn}\cdot f'(1) \tag{7a}$$

and for the second order slip model

$$f(-1)=f(+1)=-\frac{2-\sigma_v}{\sigma_v}\left(\mathrm{Kn}\cdot f'(1)+\frac{\mathrm{Kn}^2}{2}f''(1)\right) \tag{7b}$$

where the characteristic Knudsen number of the flow is defined as

$$\mathrm{Kn}=\frac{\lambda}{r\alpha} \tag{8}$$

The condition given in Eq. (6) can be replaced by the symmetry requirement $f'(0)=0$ and confine the analysis to the upper half of the wedge region. Since Eq. (5) is nonlinear, it is next solved numerically by reducing it to a system of first-order equations

$$F_0'(\eta)=F_1(\eta) \tag{9a}$$

$$F_1'(\eta)=F_2(\eta) \tag{9b}$$

$$F_2'(\eta)=-2\mathrm{Re}\alpha\cdot F_0(\eta)F_1(\eta)-4\alpha^2\cdot F_1(\eta) \tag{9c}$$

with the boundary conditions as follows:

$$F_0(0)=1 \tag{10a}$$

$$F_1(0)=0 \tag{10b}$$

$$F_0(1)=-\frac{2-\sigma_v}{\sigma_v}\mathrm{Kn}\cdot F_1(1),$$

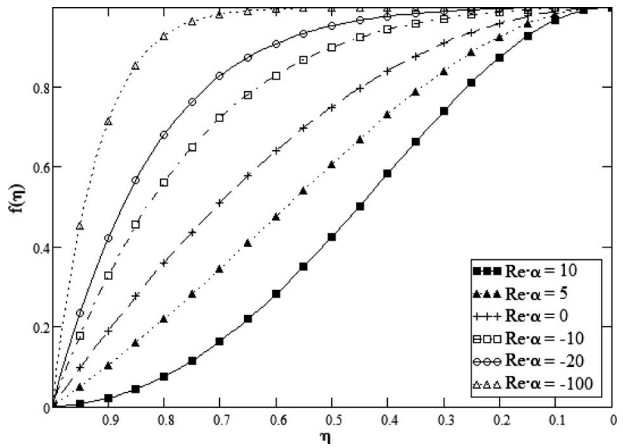

Fig. 2 Velocity profiles for the Jeffery–Hamel flow at Re≫α with no-slip boundary conditions [12]

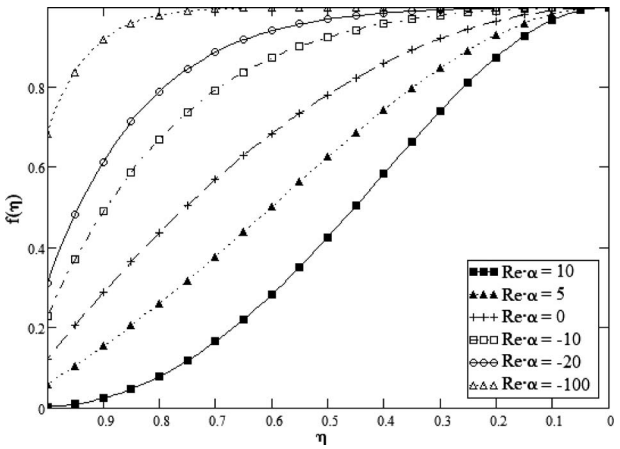

Fig. 3 Velocity profiles for the Jeffery–Hamel flow at Re≫α with first-order velocity-slip boundary condition at Kn=0.02

$$\text{or} \quad F_0(1) = -\frac{2-\sigma_v}{\sigma_v}\left(\text{Kn}\cdot F_1(1) + \frac{\text{Kn}^2}{2}F_2(1)\right) \tag{10c}$$

These equations are solved using the Runge–Kutta method by subroutine written in MATHCAD. Another parameter that is to be studied here is the skin friction coefficient C_f, which depends on the shear at the wall τ_w, which is defined as

$$\tau_w = -\mu\frac{\partial u}{\partial y} \tag{11}$$

where y is the normal to the wall.

Equation (11) is then rewritten in dimensionless form in terms of C_f and Re as follows:

$$C_f = -\frac{2}{\text{Re}}f'(\eta) \tag{12}$$

The solution of Eqs. (9) and (10) for a range of $\text{Re}\cdot\alpha$ and Kn numbers gives the velocity profiles plots, and the solution of Eq. (12) gives the skin friction coefficient. From these results the differences among the three models are found for the specified range of Kn numbers. Also the reversal of the flow concept is further investigated.

3 Results

The classical Jeffery–Hamel flow case with no-slip boundary conditions has been studied extensively with the most noticeable contribution made by Rosenhead [35], who summarized his findings from which the following conclusions have been extracted. For $\pi/2<\alpha<\pi$, a solution with pure outflow is impossible, and pure-inflow solutions are limited in certain respects. Also, for $\alpha<\pi/2$, pure inflow is always possible and tends at large Re to have boundary-layer behavior, while pure outflow is limited to certain small Re, whose approximate range is $\text{Re}<10.31/\alpha$.

Also since the most practical application of this flow is for large Re and small α in the rest of the work, the study will be concentrated on the region $\alpha<\pi/2$ and $\text{Re}\gg\alpha$. Figure 2 represents the classical Jeffery–Hamel flow solution with no-slip boundary conditions, which serves as a comparison for the next figure (Fig. 3), which recreates the same conditions but using the first-order slip model at Kn=0.02. It can be seen from the two figures that in the no-slip solution, as the name implies, the velocity at the wall is always zero, no matter what the $\text{Re}\cdot\alpha$ parameter value is, while for the first-order slip model, there is a velocity slip which is small for $\text{Re}\cdot\alpha>0$ (outflow), and the slip starts to increase as $\text{Re}\cdot\alpha$ become smaller and then negative as $\text{Re}\cdot\alpha<0$ (inflow).

In order to study the effect of the parameter $\text{Re}\cdot\alpha$ on the velocity profiles, Figs. 4–6 are generated. They show the velocity profiles resulting from the three models—the no-slip model, and the first- and second-order velocity-slip models at different $\text{Re}\cdot\alpha$ and for different Kn numbers. Figure 4 shows the velocity profiles for $\text{Re}\cdot\alpha=-10$, which is an inflow. What can be seen from this figure is that increasing the Kn number will increase the velocity slip at the wall. The difference between the no-slip model and the two slip models is small up to a Kn=0.01, after which it becomes significant. Also the difference between the first- and second-order slip models is relatively small up to about Kn=0.05, after which it becomes noticeable.

The next figure (Fig. 5) shows the velocity profiles at $\text{Re}\cdot\alpha=0$, and it can be seen here that the difference between the no-slip model and the two slip models is negligible all the way up to Kn=0.01 and becomes important only at larger values of Kn. What differentiates this figure from the one above is that, first, the slip at the wall is smaller in magnitude than in the previous figure, and second, the difference between the first-and second-order slip models is negligible across the entire Kn number range explored.

For the case of outflow (positive α), the difference between the no-slip model and the two slip models is very small for $\text{Kn}<0.05$ and also the difference between the first- and second-order slip models is negligible across the entire Kn number range explored. The exception happens when the parameter $\text{Re}\cdot\alpha$ increases significantly and approaches the critical value of 10. This is shown in Fig. 6, which shows that the velocity profiles for the three models are so close that they cannot be differentiated from one another, but the interesting thing here is that the second-order model predicts a negative slip velocity at the wall as Kn increases, which indicates reversal of the flow at that point.

Similar behavior called flow separation is a well documented case in the Jeffery–Hamel flow with no-slip boundary conditions. As it was seen in Figs. 2 and 6, for the outflow, the velocity profiles become S-shaped as a result of the change in the sign of the streamwise pressure gradient. For the case of inflow, the pressure p decreases in the direction of the flow (favorable pressure gradient) and there is no separation, while for the outflow, the pressure increases downstream (adverse pressure gradient) and causes inflection in the velocity profile until at some point a separation occurs. For the no-slip boundary conditions this separation point is a function of $\text{Re}\cdot\alpha$ and has been found by Millsaps and Pohlhausen [36] to occur at $\text{Re}\cdot\alpha=10.31$. But as it can be seen from Fig. 6, the second-order slip model predicts that the reversal of the flow analogous to the separation in the no-slip model can occur at smaller $\text{Re}\cdot\alpha$ if the Kn number is sufficiently large.

Assuming that a difference between the no-slip model and the first-order velocity-slip of 10% or more is significant enough to justify the use of the velocity-slip model, criteria for the use of the first order slip model can be set. By examining Fig. 7, it can be

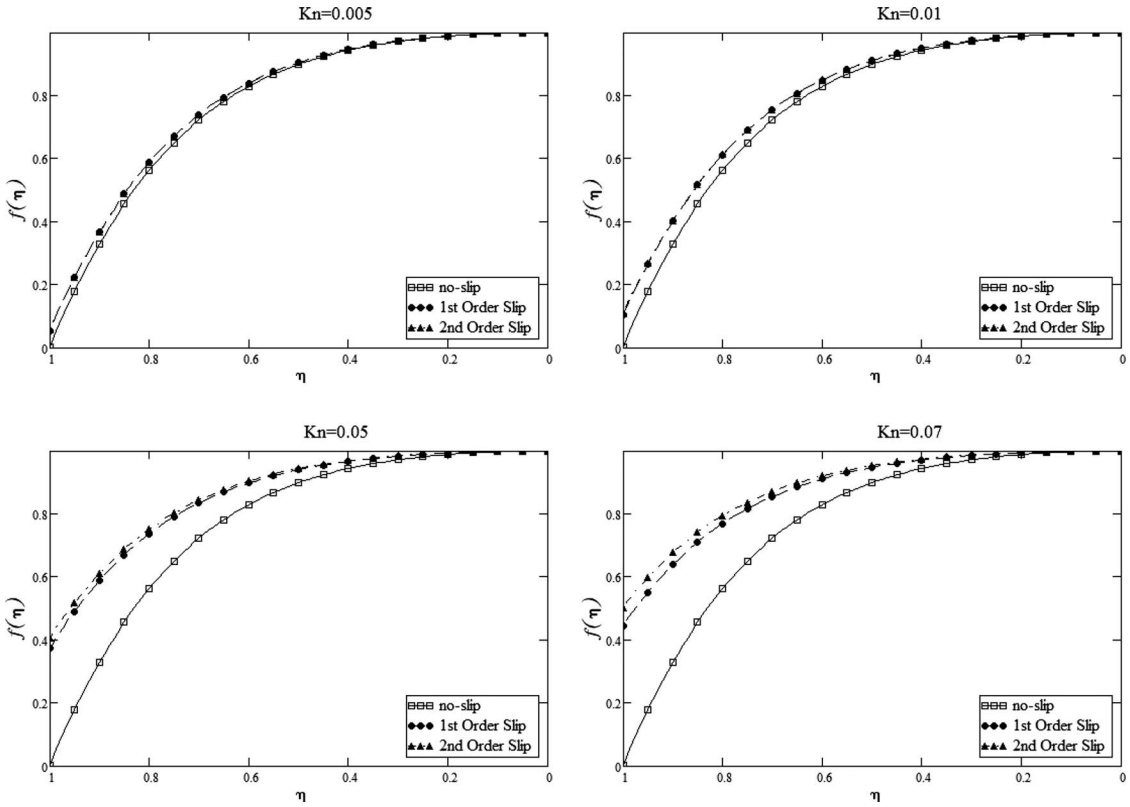

Fig. 4 Comparison of the velocity profiles for the Jeffery–Hamel flow at Re·α=−10 using the three models: no-slip, first-order, and second-order velocity-slip boundary conditions

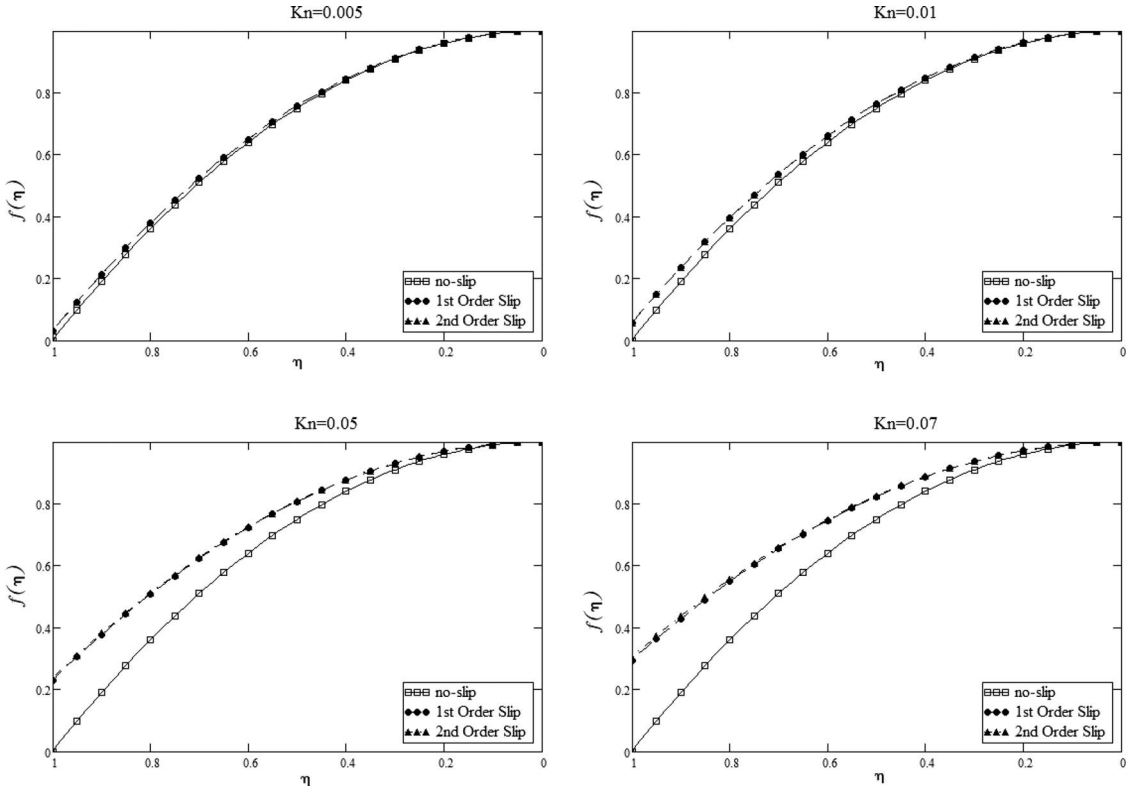

Fig. 5 Comparison of the velocity profiles for the Jeffery–Hamel flow at Re·α=0 using the three models: no-slip, first-order, and second-order velocity-slip boundary conditions

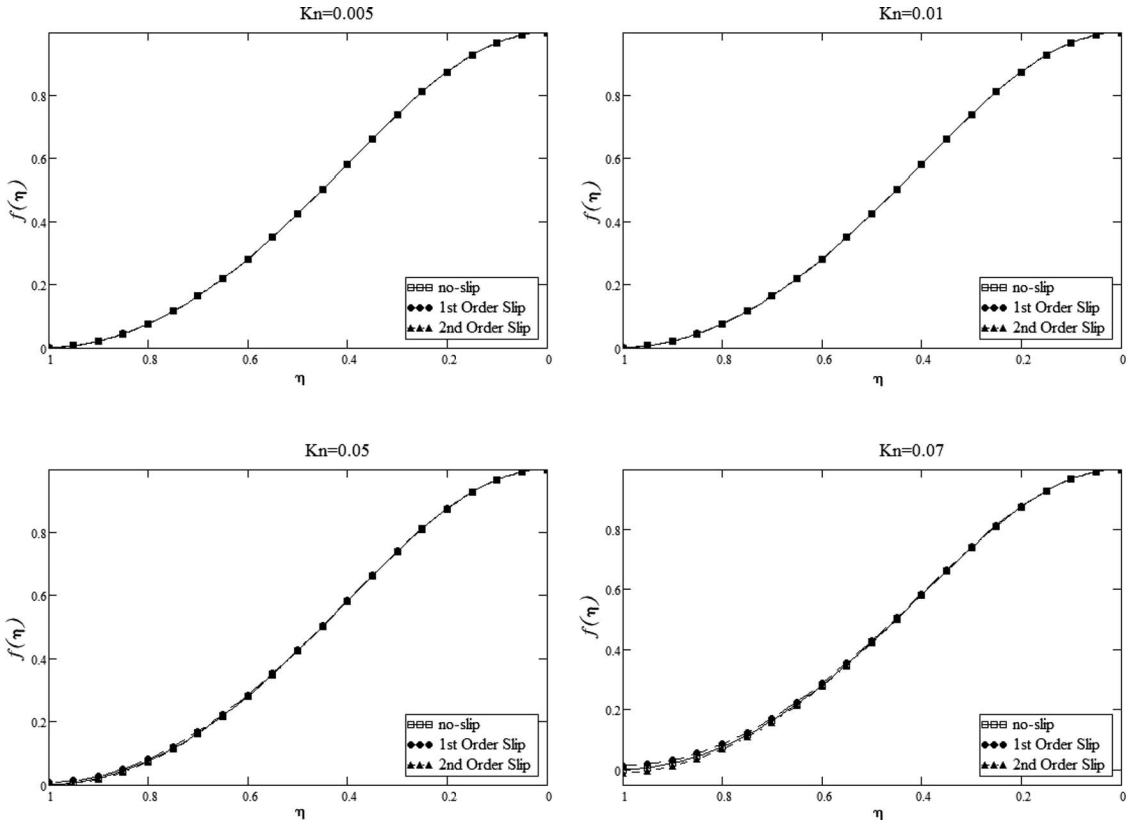

Fig. 6 Comparison of the velocity profiles for the Jeffery–Hamel flow at Re·α=+10 using the three models: no-slip, first-order, and second-order velocity-slip boundary conditions

seen that for Re·α=−10, the difference reaches 10% at Kn =0.01, for Re·α=−5 at Kn=0.012, for Re·α=0 at Kn=0.02, and for Re·α=+5 at Kn=0.04. As for the Re·α=+10, the difference between the three models is negligible but since the second-order slip model predicts the reversal, it will be studied more extensively later.

Also of interest is the difference between the first- and second-order slip models. This is why the normalized difference between the two models is shown in Fig. 8. Ignoring the line which represents the difference at Re·α=+10 as it represents the case where reversal of the flow occurs, the next line representing the difference for outflow at Re·α=+5 is examined. Using the same 10% difference criteria, it can be seen that the second-order model becomes necessary only for Kn>0.09, which is very close to the upper limit of the range, in which the Navier–Stokes equation with slip boundary conditions is applicable. For Re·α=0, the difference between the two models never reaches 10%, so for this case, the first-order slip model will be sufficient. As for the inflow cases at Re·α=−5 and −10, the difference becomes significant at Kn=0.075 and 0.052, respectively.

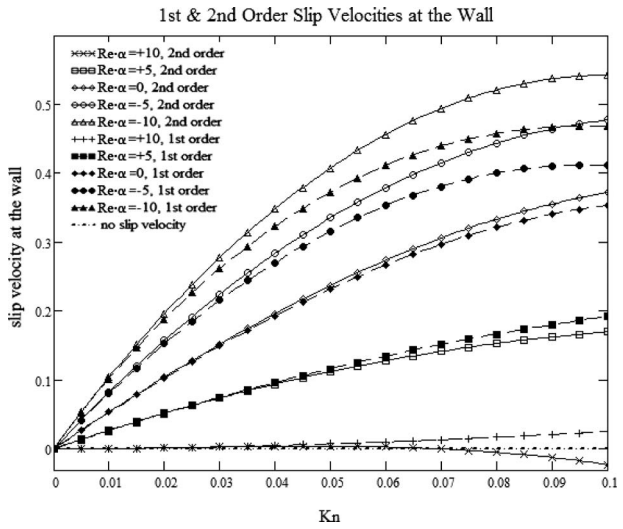

Fig. 7 First- and second-order model predicted slip velocities at the wall

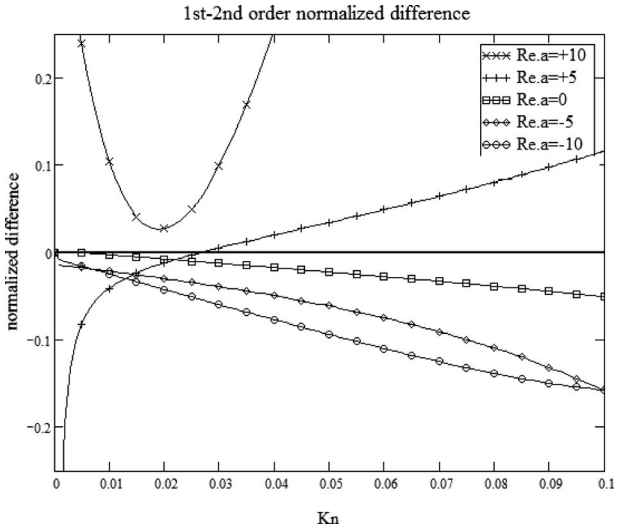

Fig. 8 Normalized difference between the first- and second-order model predicted velocity slips at the wall

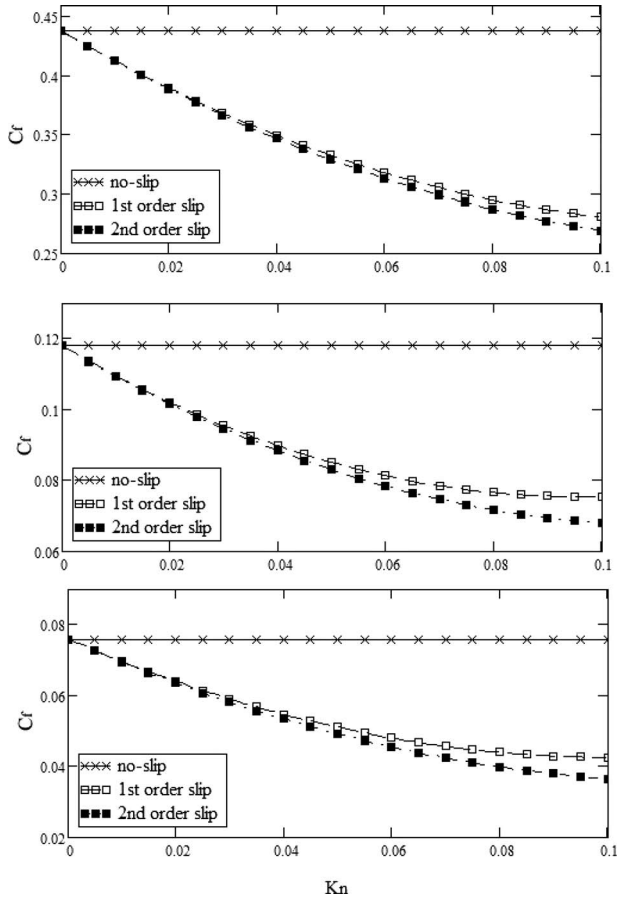

Fig. 9 Friction coefficient C_f comparison at $\alpha=-0.1$ and different Re: (*a*) for Re=10, (*b*) for Re=50, and (*c*) for Re=100

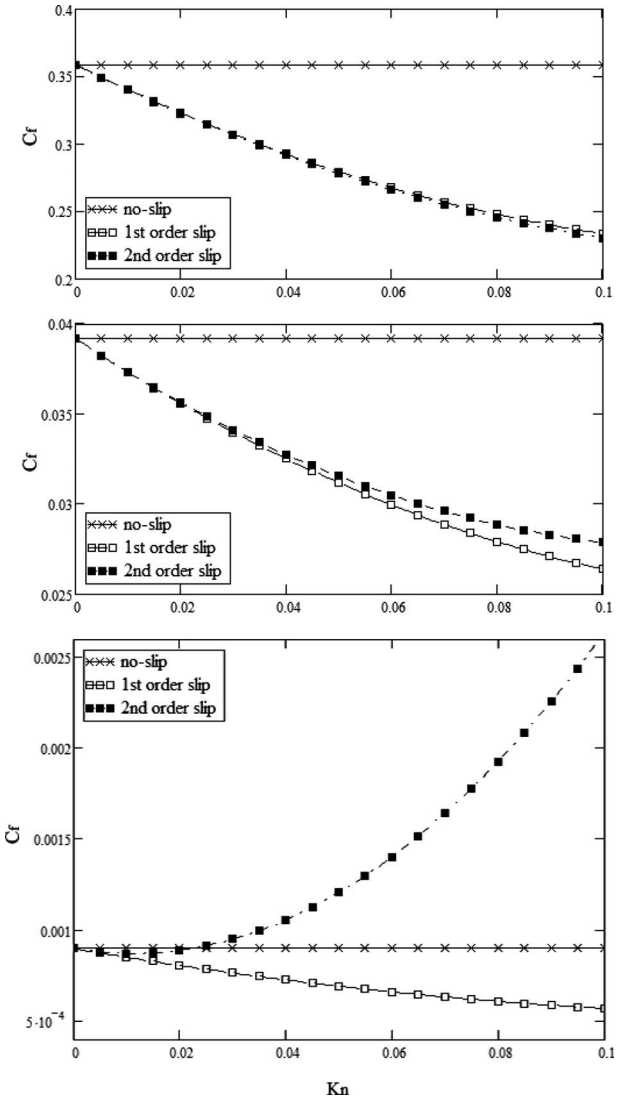

Fig. 10 Friction coefficient C_f comparison at $\alpha=+0.1$ and different Re: (*a*) for Re=10, (*b*) for Re=50, and (*c*) for Re=100

Next, the effect of the Kn number on the skin friction coefficient C_f is examined. Figure 9 shows the skin friction coefficient C_f for an inflow with different values of the Re number, while Fig. 10 represents C_f for an outflow. As it can be seen for the inflow, the two velocity-slip models result in reduced friction at the wall with the second-order slip model always resulting in lower friction coefficient values. On the other hand, for the outflow cases, it is seen that at small Re, both models show lower friction coefficient than the no-slip model, and the second-order slip model predicts lower values than the first-order model. As Re increases to Re=50, the second-order model results in values larger than the first-order model but still lower than the no-slip model. Finally, as the Re number increases to Re=100, the values of C_f predicted by the second-order slip model drastically increases and become even larger than the values for the no-slip model. This strange behavior can be attributed to the reversal of the flow at the wall, which only the second-order slip model predicts.

Due to the importance of the flow reversal concept on the analysis, so far it was further investigated and summarized in Figs. 11 and 12. The first one shows the velocity slip at the wall as predicted by the second-order velocity-slip model, for different values of Kn as a function of $\mathrm{Re}\cdot\alpha$. It shows that as the Kn number increases, the $\mathrm{Re}\cdot\alpha$ value for which the reversal occurs decreases. For Kn=0.01 the reversal occurs at about $\mathrm{Re}\cdot\alpha=10.2$, which is very close to the results for the no-slip solution, while for Kn=0.1, the reversal occurs at $\mathrm{Re}\cdot\alpha=8.8$. On the other hand, Fig. 12 represents the slip velocity at the wall for different $\mathrm{Re}\cdot\alpha$ as a function of the Kn number. It shows that the larger the $\mathrm{Re}\cdot\alpha$ value is, the smaller Kn number is needed for flow reversal to occur.

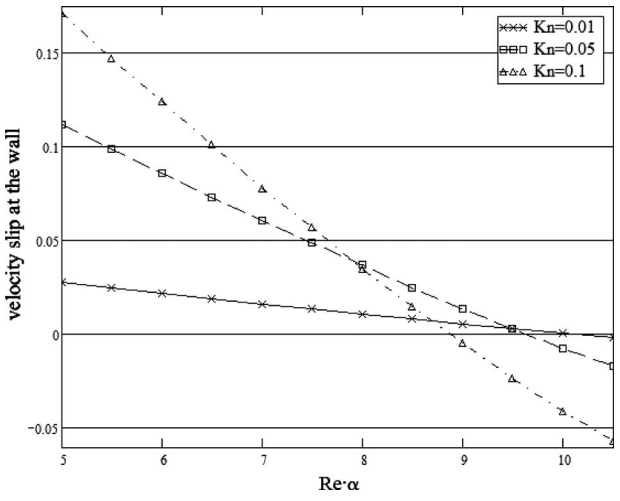

Fig. 11 Second order model predicted velocity slip at the wall for different Kn numbers as a function of $\mathrm{Re}\cdot\alpha$

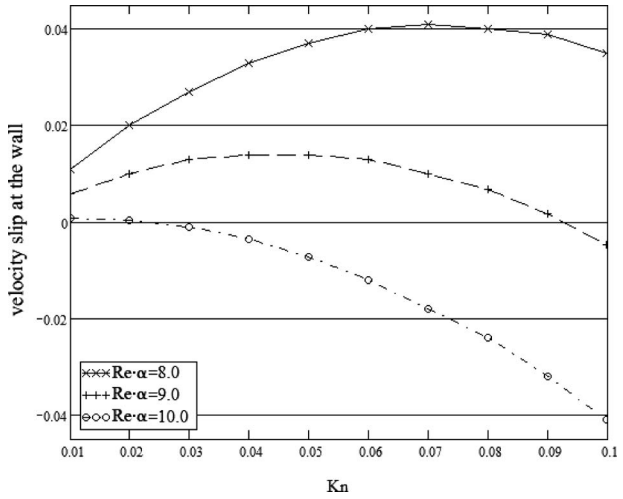

Fig. 12 Second order model predicted velocity slip at the wall for different $\mathrm{Re}\cdot\alpha$ as a function of the Kn number

4 Conclusions

In the present work, the Jeffery–Hamel flow case has been studied using both the first- and second-order velocity-slip boundary condition models, and then compared with the no-slip boundary condition solution. The aim of this paper is to observe the behavior of the flow predicted by the two slip models and to try and establish criteria for using the two velocity-slip models. The study concentrates on investigating the effect the change in the Kn number has on the velocity profiles, magnitude of slip at the wall, and skin friction coefficient. A Jeffery–Hamel flow is a radial flow caused by a line source or sink. The major factor in this kind of flows is the combined $\mathrm{Re}\cdot\alpha$ factor according to which the flow can be divided into two categories, i.e., inflow and outflow. When $\mathrm{Re}\cdot\alpha<0$ the flow is toward a sink and is called the inflow, and when $\mathrm{Re}\cdot\alpha>0$ the flow is outward of a source and is called the outflow.

For the inflow case, it was found that due to the favorable pressure gradient, the differences between the three models studied increase significantly as the Kn number increases, and according to that, the three Kn number regions can be established. The first is the region where there is no need to use any velocity-slip model as the no-slip model is accurate enough. The second is the region where the first-order velocity slip model is sufficient, and the third region is where only the second-order velocity-slip model will suffice. As an example, for the case of $\mathrm{Re}\cdot\alpha=-10$, these regions are as follows: for $0<\mathrm{Kn}<0.01$, the no-slip boundary conditions model is sufficient, for $0.01<\mathrm{Kn}<0.05$, the first-order velocity-slip model becomes necessary, and for $0.05<\mathrm{Kn}<0.1$, the second-order velocity-slip model will have to be used.

In the outflow case, the things stand a little more complex, as for $0<\mathrm{Re}\cdot\alpha<8$, the difference between the no-slip model and the two slip models is much smaller than for the inflow case. For example, at $\mathrm{Re}\cdot\alpha=+5$, the difference becomes significant only at about $\mathrm{Kn}>0.04$, so up to then, the no-slip model will give acceptable results. Also the difference between the first- and second-order slip models is negligible for almost the entire range of Kn numbers. But as $\mathrm{Re}\cdot\alpha$ parameter becomes larger, and for relatively large Kn numbers, the adverse pressure gradient causes the flow at the wall to separate at $\mathrm{Re}\cdot\alpha$ values lower than 10.31, which is the value obtained for the no-slip boundary conditions model. This fact is predicted only by the second-order velocity-slip model for $9<\mathrm{Re}\cdot\alpha<10.31$. So for outflow cases near the flow reversal region, the second-order velocity-slip model should always be used.

It was also found that increasing the Kn number decreases the skin friction coefficient C_f, which is calculated using the two velocity-slip models in all cases except for when flow reversal occurs, as when the velocity at the wall is reversed. As predicted by the second-order velocity-slip model, this factor increases.

Nomenclature

C_f = skin friction coefficient
Kn = Knudsen number, $=\lambda/r\alpha$
p = pressure
Re = Reynolds number, $=u_{\max}r\alpha/\nu$
r = radial coordinate
$u_{\max}$ = centerline velocity
u_r = radial velocity
α = wall angle
η = dimensionless angle, $=\theta/\alpha$
θ = polar coordinate angle
λ = mean free path length
μ = viscosity
ν = kinematic viscosity
ρ = density
σ_v = tangential momentum accommodation coefficient
τ_w = shear stress at the wall

References

[1] Al-Nimr, M. A., Naji, M., and Arpaci, V., 2000, "Non-Equilibrium Entropy Production Under the Effect of Dual-Phase Lag Heat Conduction Model," ASME J. Heat Transfer, **122**, pp. 217–223.
[2] Chen, Y., Kang, S., Tuh, W., and Hsiao, T., 2004, "Experimental Investigation of Fluid Flow and Heat Transfer in Microchannels," Tamkang Journal of Science and Engineering, **7**(1), pp. 11–16.
[3] Choquette, S. F., Faghri, M., Kenyon, E. J., and Sunden, B., 1996, "Compressible Fluid Flow in Micron-Sized Channels," *Proceedings of the National Heat Transfer Conference*, Vol. 5, pp. 25–32.
[4] Colin, S., Lalonde, P., and Caen, R., 2004, "Validation of a Second-Order Slip Flow Model in Rectangular Microchannels," Heat Transfer Eng., **25**(3), pp. 23–30.
[5] Gad-el-Hak, M., 1999, "The Fluid Mechanics of Microdevices—The Freeman Scholar Lecture," ASME J. Fluids Eng., **121**, pp. 5–33.
[6] Gad-el-Hak, M., 2002, "Flow Physics in Microdevices," *The Handbook of MEMS*, CRC, Boca Raton, FL.
[7] 2002, *The Handbook of MEMS*, M. Gad-el-Hak, ed., CRC, Boca Raton, FL.
[8] Lauga, E., 2005, "Microfluidics: The No-Slip Boundary Condition," *Handbook of Experimental Fluid Dynamics*, J. Foss, C. Tropea, and A. Yarin, eds., Springer, New York, Chap. 15.
[9] Haddad, O., Al-Nimr, M., and Abuzaid, M., 2005, "The Effect of Frequency of Fluctuating Driving Force on Basic Gaseous Micro-Flows," Acta Mech., **179**, pp. 249–259.
[10] Harley, J. C., Huang, Y., Bau, H., and Zemel, J. N., 1995, "Gas Flows in Micro-Channels," J. Fluid Mech., **284**, pp. 257–274.
[11] Ho, C., and Tai, Y., 1998, "Micro-Electro-Mechanical Systems (MEMS) and Fluid Flows," Annu. Rev. Fluid Mech., **30**, pp. 579–612.
[12] Karniadakis, G., and Beskok, A., 2002, *Micro Flows Fundamentals and Simulation*, Springer, New York, pp. 32–75.
[13] Roy, S., Raju, R., Chuang, H. F., Cruden, B. A., and Meyyappan, M., 2003, "Modeling Gas Flow Through Microchannels and Nanopores," J. Appl. Phys., **93**(8), pp. 4870–4879.
[14] Tuckerman, D. B., and Pease, R. F. W., 1981, "High-Performance Heat Sinking for VLSI," IEEE Electron Device Lett., **2**, pp. 126–129.
[15] Jiang, X. N., Zhou, Z. Y., Yao, J., Li, Y., and Ye, X. Y., 1995, "Micro-Fluid Flow in Microchannel," *Proceedings of the Transducers '95: Eurosensor IX, Eighth International Conference on Solid-State Sensors and Actuators, and Eurosensors IX*, Sweden, pp. 317–320.
[16] Flockhart, S. M., and Dhariwal, R. S., 1998, "Experimental and Numerical Investigation Into the Flow Characteristics of Channels Etched in Silicon," ASME J. Fluids Eng., **120**, pp. 291–295.
[17] Sharp, K. V., Adrian, R. J., and Beebe, D. J., 2000, "Anomalous Transition to Turbulence in Microtubes," *Proceedings of the International Mechanical Engineers Congress and Exposition, Fifth Micro-Fluidic Symposium*, Orlando, FL, Nov. 5–10.
[18] Peiyi, W., and Little, W. A., 1983, "Measurement of Friction Factors for the Flow of Gases in Very Fine Channels Used for Micro Miniature Joule-Thomson Refrigerators," Cryogenics, **23**, pp. 273–277.
[19] Peng, X. F., Peterson, G. P., and Wang, B. X., 1994, "Frictional Flow Characteristics of Water Flowing Through Rectangular Microchannels," Exp. Heat Transfer, **7**, pp. 249–264.
[20] Mohiuddin Mala, Gh., and Li, D., 1999, "Flow Characteristics of Water in Microtubes," Int. J. Heat Fluid Flow, **20**, pp. 142–148.
[21] Weilin, Q., Mohiuddin Mala, Gh., and Li, D., 2000, "Pressure-Driven Water Flows in Trapezoidal Silicon Microchannels," Int. J. Heat Mass Transfer, **43**,

pp. 353–364.
[22] Papautsky, I., Brazzle, J., Ameel, T., and Frazier, A. B., 1999, "Laminar Fluid Behavior in Microchannels Using Micropolar Fluid Theory," Sens. Actuators, A, **73**, pp. 101–108.
[23] Papautsky, I., Gale, B. K., Mohanty, S., Ameel, T. A., and Frazier, A. B., 1999, "Effects of Rectangular Microchannel Aspect Ratio on Laminar Friction Constant," *Proceedings of the SPIE Conference on Microfluidic Devices and Systems II*, Santa Clara, CA, Vol. 3877, pp. 147–158.
[24] Choi, S. B., Barron, R. F., and Warrington, R. O., 1991, "Fluid Flow and Heat Transfer in Microtubes," *Micro-mechanical Sensors, Actuators, and Systems*, ASME, New York, **DES-Vol. 32**, pp. 123–134.
[25] Pfahler, J., Harley, J., Bau, H., and Zemel, J., 1990, "Liquid Transport in Micron and Submicron Channels," Sens. Actuators, A, **21–23**, pp. 431–434.
[26] Pfahler, J., Harley, J., Bau, H. H., and Zemel, J., 1990, "Liquid and Gas Transport in Small Channels," *Proceedings of the ASME Winter Annual Meeting on Microstructures, Sensors and Actuators*, Dallas, TX, Vol. 19, pp. 149–157.
[27] Pfahler, J., Harley, J., Bau, H., and Zemel, J. N., 1991, "Gas and Liquid Flow in Small Channels," *Proceedings of the ASME Winter Annual Meeting on Micromechanical Sensors, Actuators and Systems*, Atlanta, GA, Vol. 32, pp. 49–59.
[28] Yu, D., Warrington, R., Barron, R., and Ameel, T., 1995, "An Experimental and Theoretical Investigation of Fluid Flow and Heat Transfer in Microtubes," *Proceedings of the ASME/JSME Thermal Engineering Joint Conference*, Maui, HI, Mar. 19–24, pp. 523–530.
[29] Pozrikidis, C., 2005, "Effect of Membrane Thickness on the Slip and Drift Velocity in Parallel Shear Flow," J. Fluids Struct., **20**(2), pp. 177–187.
[30] Pozrikidis, C., 2004, "Boundary Conditions for Shear Flow Past a Permeable Interface Modeled as an Array of Cylinders," Comput. Fluids, **33**(1), pp. 1–17.
[31] Wilding, P., Pfahler, J., Bau, H. H., Zemel, J. N., and Kricka, L. J., 1994, "Manipulation and Flow of Biological Fluids in Straight Channels Micromachined in Silicon," Clin. Chem., **40**, pp. 43–47.
[32] White, F. M., 1991, *Viscous Fluid Flow*, 2nd ed., McGraw-Hill, New York, pp. 25–189.
[33] Jeffery, G. B., 1915, "The Two-Dimensional Steady Motion of a Viscous Fluid," Philos. Mag., **29**, pp. 455–465.
[34] Hamel, G., 1917, "Spiralförmige Bewegung zäher Flüssigkeiten," Jahresber. Dtsch. Math.-Ver., **25**, pp. 34–60.
[35] Rosenhead, L., 1940, "The Steady Two-Dimensional Radial Flow of Viscous Fluid Between Two Inclined Planes," Proc. R. Soc. London, Ser. A, **175**, pp. 436–467.
[36] Millsaps, K., and Pohlhausen, K., 1953, "Thermal Distribution in Jeffery-Hamel Flows Between Nonparallel Walls," J. Aeronaut. Sci., **20**, pp. 187–196.